International Journal of Heat and Mass Transfer 55 (2012) 7487–7498

Contents lists available at SciVerse ScienceDirect

International Journal of Heat and Mass Transfer

journal homepage: www.elsevier.com/locate/ijhmt

Enhanced heat transfer performance of alumina sponge-like nano-porous structures through surface wettability control in nucleate pool boiling

Bong June Zhang [a], Kwang Jin Kim [a,b,*], Hyungkee Yoon [c]

[a] Department of Mechanical Engineering, University of Nevada, Reno, NV 89557, USA
[b] Department of Mechanical Engineering, University of Nevada, Las Vegas, NV 89154, USA
[c] Korea Institute of Energy Research, 152 Gajeong-ro, Yuseong-gu, Daejeon 305-343, South Korea

ARTICLE INFO

Article history:
Received 10 January 2012
Received in revised form 18 July 2012
Accepted 18 July 2012
Available online 22 August 2012

Keywords:
Nano-porous surfaces
Aluminum oxide
Anodizing
Surface wettability
Nucleate pool boiling heat transfer enhancement

ABSTRACT

For several decades, a porous surface has been recognized as an efficient medium to increase boiling performance in a nucleate boiling regime. Most feasible porous surfaces have been studied in millimeter and micron-sized domains. It has been believed that a higher wall superheat is required to commence incipient nucleate boiling under a submicron regime. In this study, we demonstrate that a significantly enhanced pool boiling heat transfer is observed in a submicron regime through three dimensionally interconnected hybrid pores: the Alumina sponge-like nano-porous structure (ASNPS). The structural uniqueness of the ASNPS leads to an enlarged surface area, increases the potential number of the active nucleation site density, and improves the vapor–liquid menisci through the reentrant pore. Simultaneously, by changing the surface wettability with a hydrophobic self-assembled monolayer (SAM) coating, the number of active nucleation site density is improved. Eventually, the combination of the ASNPS and hydrophobic SAM coating can achieve substantial heat transfer coefficient (HTC) enhancement in the nucleate boiling. Also, the thickness of the ASNPS is a critical issue to adequately augment the HTC in pool boiling. The thickness of the ASNPS is optimized by examining the boiling performance of the ASNPS fabricated in different amounts of anodizing times. A classical mechanistic model from literature was modified and compared with the experimentally obtained data. The modified mechanistic model – with the combination of forced-convection and thin liquid film evaporation – showed reasonable predictions.

1. Introduction

Ideal surface geometries that enhance pool boiling performance have been recognized as a critical issue to increase the performance of the boiling heat transfer. Various specially designed surface geometries have been considered (Table 1). In 1931, Jakob and Fritz observed an improvement in the boiling heat transfer coefficient by using a square grid of machined grooves [1]. In 1950s and 1960s, there were several relevant studies reporting an augmentation in the boiling heat transfer by roughening the heating surface. For instance, Corty and Foust reported a boiling heat transfer enhancement on grit-roughened surfaces in 1955 [2]. However, these surface-treated structures showed a significant aging effect within a few tests. In order to overcome the surface aging, some of researchers began to focus on more efficient surface geometries such as a reentrant cavity. Marto and Rohsenow carried out a boiling test with copper block, which had 12 reentrant cavities [3]. Their study highlighted the performance-potential of reentrant cavities and porous coatings. Since their investigation, some innovators in the industry have been motivated to develop commercially feasible reentrant cavities and porous coatings. In the 1970s and 1980s, various mechanical and chemical approaches in pool boiling created novel surface structures. Nakayama et al. [4] proposed porous surfaces, which consisted of regularly distributed triangular pores. By creating three dimensionally-interconnected pores, he expected additional vaporization of liquid inside the pores. Among the various diameters of pores (0.03–0.2 mm), he observed heat transfer improvement on the surface structures with 0.1 mm diameter pores. Bergles and Chyu [5] reported enhanced pool boiling results utilizing a metallic porous media made of copper particles with various diameters. The pore diameter of the heating surface was 74 – 404 μm. They characterized their porous structure as a "vapor chimney", acted as of liquid channel where evaporation occurred. From two studies, the concept of liquid evaporation inside pores began to be widely accepted in the pool boiling phenomena. Continued studies demonstrated a wide variety of surface fabrication methods: a plasma coating [6], a unique coating [7], a fused inorganic pore [8], and copper forms [9].

The majority of the porous structures in previous studies were in the submillimeter and/or micron domain. For example, Hus's

* Corresponding author at: Department of Mechanical Engineering, University of Nevada, Las Vegas, NV 89154, USA. Tel.: +1 702 774 1419.
E-mail address: Kwang.kim@YNLV.edu (K.J. Kim).

0017-9310/$ - see front matter © 2012 Elsevier Ltd. All rights reserved.
http://dx.doi.org/10.1016/j.ijheatmasstransfer.2012.07.053

Nomenclature

A	surface area [m^2]
Bo	Bond number
c_p	heat capacity [kJ/kg]
d	diameter [m]
f	frequency [1/s]
g	gravitation acceleration [m/s^2]
h	heat transfer coefficient [kW/m^2 K]
I	current [A]
i	enthalpy [J/kg]
Ja	Jakob number
k	thermal conductivity [W/m K]
L	length of test section [m]
N	active nucleation site density [$1/m^2$]
P	pressure [Pa]
Pr	Prandtl number
Q	input power [W]
q''	heat flux [W/m^2]
r	radius [m]
t	time [s]
T	temperature [K]
ΔT	temperature difference [K]
V	voltage [V]
y	distance from heating surface [m]

Greek letters

β	cavity mouth half angle [°]
δ	thin liquid film thickness [m]
Δ	difference
μ	viscosity [Pa s]
ρ	density [kg/m^3]
ϑ	contact angle [°]
σ	surface tension [N/m]

Subscripts

A	the number of active nucleation site density
a	*advancing angle*
b	bubble
bottom	at the bottom of heater section
c	cavity
l	liquid
i	inside
left	at the left of heater section
lv	liquid–vapor
ls	liquid–solid
max	maximum
min	minimum
o	outside
p	pore
r	*receding angle*
right	at the right of heater section
s	solid
sat	saturation
sv	solid–vapor
sl	solid–liquid
sub	subcooling
thermo	thermocouple
top	at the top of heater section
v	vapor
w	wall

model [10] deals with the size range of active cavities for incipient boiling in submicron domain boiling. Also, it should be noted that nano-surface patterning with high precision on a specific boiling area has been another challenge to overcome. Recently, these technical issues have been defined by researchers who opened a new era of the pool boiling in a nano regime. In 2006, Launay et al. [11] examined various silicon surfaces with a Carbon Nano Tube (CNT) coating on the pool boiling heat transfer in PF5060 and water. He observed that the CNT, with the inner diameter of the CNTS being 10–20 nm and the spacing between individual nanotubes 50–70 nm, enabled nano-structured surface to improve the pool boiling heat transfer at a low superheat regime. In 2008, Li et al. [12] fabricated a one-dimensionally grown copper surface utilizing an electro-deposition method and observed a significantly enhanced heat transfer performance using such a nano surface.

In addition to the fabrication techniques to create and manipulate porous coatings, the wetting control was investigated to improve the pool boiling heat transfer. In 1960, Griffith and Wall made a non-wetting surface with a Teflon coating [13]. They reported that the non-wetting cavities led to an incipience of boiling water at a lower superheat. Similarly, Hummel [14], Gaetner [15] and Vachon et al. [16] observed a considerably enhanced heat transfer by making non-wetting cavities. In 1993, Wang and Dhir [17] improved the active nucleation site density by controlling the surface-wetting of the cavities by technically restricting the contact to a designated angle regime ($10° < \vartheta < 90°$).

In this study, we report a novel alumina sponge-like nanoporous surface (ASNPS), which is fabricated through a unique anodization process. Anodizing is feasible to many affordable industrial processes that create high-end surface patterning. The process is applicable for various materials such as aluminum [18], titanium [19], and copper [20]. The ASNPS has several unique structural features. First, it has hybrid pores with a diameter range of 100–500 nm. Each pore plays different roles in the nucleate

Table 1
Various approaches to fabricate porous structure in pool boiling.

References	Boiling regimes	Surface treatment	Pore size	Fluid
Nakayama et al. [4]	Nucleate	Microchannel	0.2–0.03 mm	R-11
Bergles and Chu [5]	Nucleate	Porous Cu	74–44 μm	Water
Hshieh and Ke [32]	Nucleate	Plasma coating (Mo, Cu)	4 μm	R-134
Cieslinski [33]	Nucleate	Sand blasting	0.3–4 μm	Water
Rainey and You [34]	Nucleate	ABM coating (aluminum/brushable ceramic epoxy/MEK)	1–20 μm	FC-72
Kim et al. [7]	Nucleate	DOM (diamond particles/omegabond 101 epoxy binder/Methyl-ethyl-ketone carrier		Water
Li et al. [12]	Nucleate	Cu deposition	50 nm	Water
Mori and Okuyama [8]	Nucleate	Fused inorganic oxides (Al_2O_3–SiO_2–TiO_2)	1.3 mm	Water
Furberg et al. [22]	Nucleate	Cu electrodeposition	0.1–1 um	Water
El-Genk et al. [35]	Nucleate	Porous Cu cage	30–60 μm	PF-5060
Yang et al. [9]	Nucleate	Cu foam	0.77–2.76 mm	Water
Lee et al. [23]	Nucleate	Porous alumina	20–70 nm	Water

boiling. A smaller pore (<100 nm) can commence the incipience of boiling through vapor entrapment and the generated vapor can be transported into a larger pore (>500 nm). Second, the ASNPS has three-dimensionally interconnected pore networks, which can play the similar role of reentrant cavities, effectively entrapping vapor and reducing the wall superheat by boiling at a low superheat. Third, it actively pumps the liquid in and out of the pore when a bubble detaches from the surface. The capillary-assisted liquid suction can provide fresh water and reduces the wall superheat. And fourth, the interconnected networks provide a much-enhanced surface area and an increased number of active nucleate site densities. In addition to the unique porous structure, the surface wettability is modified using the Self-Assembled Monolayer (SAM). By using the SAM coating, the intrinsic water contact angle (WCA) of the ASNPS ($\vartheta \sim 50^\circ$) dramatically changes into hydrophobic form ($\vartheta \sim 150^\circ$). Eventually, we demonstrate that the combination of the ASNPS and the SAM coating achieves a dramatic heat transfer coefficient (HTC) enhancement in the nucleate pool boiling in water.

2. Experimental

2.1. Pool boiling experimental setup and procedure

The nucleate pool boiling experimental setup is schematically illustrated in Fig. 1. Dimensions of the rectangular pool boiling chamber are 101.6 mm in width, 101.6 mm in height, and 177.8 mm in length. Both ends of the pool boiling chamber consisted of Teflon plates, each with a 1.27 mm in thickness. O-rings were used on Teflon plates to ensure sealing. The boiling chamber was thoroughly insulated with 5 mm of Styrofoam and 20 mm of glasswool to prevent possible heat loss to the surrounding environment. An aluminum alloy (Al 6061) rod, with 19.1 mm in diameter and 101.6 mm in length, was used to heat the chamber. A 9.5 mm long cartridge heater (McMaster Carr 120 V, 400 W) was inserted into the center hole of the rod with a high thermal conductive paste (Omega 201) to heat the test section (Fig. 1). Four holes, each 2.4 mm in diameter and 70.0 mm in depth were mechanically drilled 90° apart at the top, middle, and bottom along the periphery of the heater. T-type thermocouples (Omega) were inserted into these holes with the thermal paste (Omega 201). An AC variable transformer supplied the controlled amount of power to the cartridge heater. The output voltage and the current were measured with highly accurate digital millimeters (Agilent 34410A and Fluke 87 V). In order to condense the vapor generated from the pool boiling chamber, a reflux condenser with a constant temperature controller (Polyscience) was used. Temperature data from the aluminum heater and the boiling pool (water) was obtained from the inserted T-type thermocouples. All information was acquired using an IOtech data acquisition system.

The experimental procedure was performed in the following order: the pool boiling chamber was filled with distilled water and slowly heated up to a pre-determined saturation temperature (T_{sat}). In order to remove dissolved gases, the pool boiling chamber was continually heated for two hours. The voltage was gradually increased internally in 4 V intervals from 20 V to 136 V. The experiments were carried out under a steady, atmospheric pressure state. The pool temperature was maintained within 0.8 °C of T_{sat}.

2.2. Preparation of alumina sponge-like nano-porous surface (ASNPS)

The porous feature size made by anodizing covers from a few nano-meters to sub-millimeter regime with respect to anodizing voltage, temperature, and electrolytes. Typically, under certain

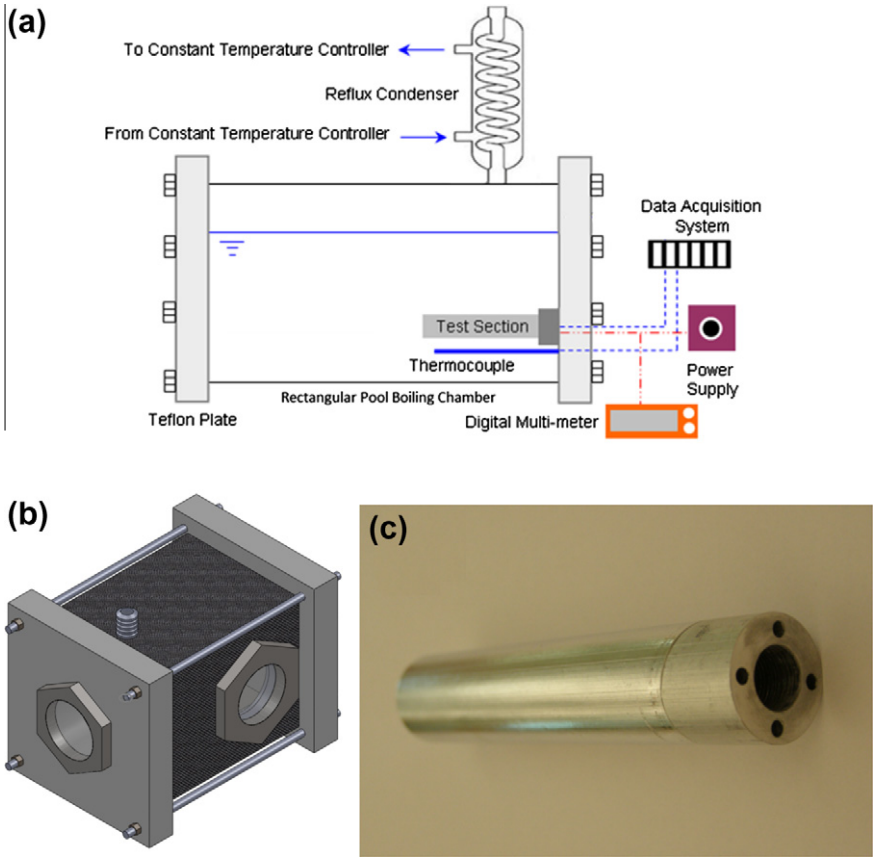

Fig. 1. Pool boiling experimental setup: (a) schematic illustration of data acquistion, (b) pool boiling chamber, and (c) Al 6061 heater section.

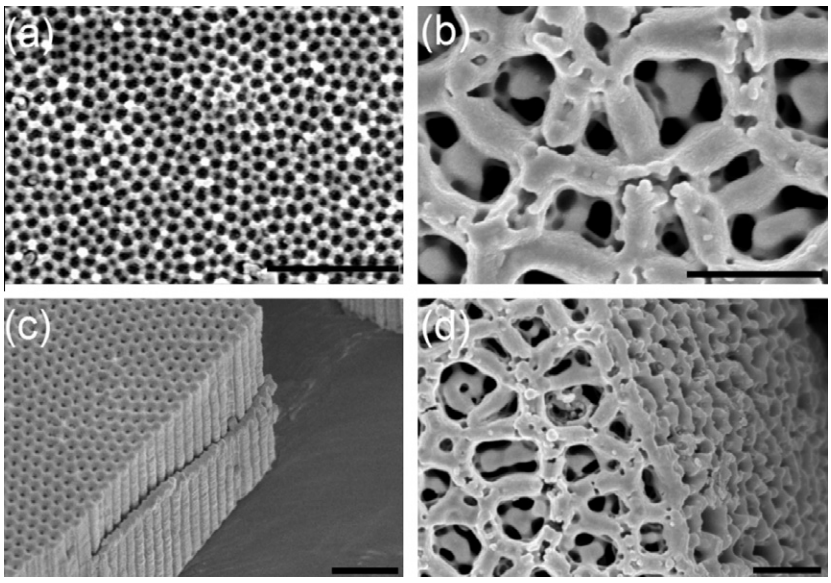

Fig. 2. Al 6061 NPS: (a) in 0.3 M H_2SO_4 at 20 V, (b) in 0.3 M H_3PO_4 at 140 V, (c) and (d) cross-sectional view of (a) and (b), respectively. Scale bar represents 500 nm.

conditions, a pore is grown in a one-dimensional direction (top to bottom) with a specific pore diameter. As shown in Fig. 2(a), hexagonally-packed, honeycomb-like porous structures are observed within the limited regime (at 25 V in 0.3 M sulfuric acid at 5 °C). In this study, three dimensionally interconnected ASNPS were created in 0.3 M phosphoric acid at 140 V in as shown Fig. 2(b). An aluminum 6061 (Al 6061) heater section was degreased and electro polished in a perchloric acid and ethanol solution (volume% 1:4): the heater section was thoroughly rinsed with ethanol several times and anodized in 0.3 M phosphoric acid at 5 °C at 140 V. After first anodizing, the alumina porous structure was etched in an aqueous ferric chloride solution at 50 °C. The anodizing was carried out under the same conditions for 2 h. Alumina pore was widened in a 1.0 M phosphoric acid for 40 min. The heater section was thoroughly rinsed with water and dried in an oven at 95 °C for over 5 h. The result was a hybrid porous structures consisting of smaller pores ($d_p \sim 100$ nm) and larger pores ($d_p \sim 500$ nm). These phenomena are observed for Al 6061 at a high voltage regime (>100 V).

2.3. Surface wettability control: hydrophobic ASNPS

The original water contact angle (WCA) of the ASNPS was ~50°, lower than a plain aluminum surface (~85°). In order to make a hydrophobic surface, the SAM was introduced. The ASNPS heater section was first immersed in an aqueous peroxide solution (25% by volume) for 30 min at 50 °C. The heater section was thoroughly rinsed with water several times. To remove residues of aqueous peroxide solution inside the pore, the heater section was immersed in deionized water for 30 min at 50 °C. The heater section was thoroughly dried using sterile, compressed air. In order to make a hydrophobic surface, the heater section was immersed in a 0.2 M 1-dodecanethiol ethanol solution for 2 h at 50 °C. After the SAM process, the heater section was thoroughly rinsed with ethanol and dried in the oven for over 5 h at 95 °C. The surface of the SAM coated ASNPS (SASNPS) dramatically changed into a hydrophobic surface (~150°), as shown in Fig. 3(b).

2.4. Data reduction

The input power supplied to cartridge heater of test section was estimated by Ohm's law in Eq. (1):

$$Q = VI \tag{1}$$

where Q, V, and I represent power, voltage, and current, respectively.

The boiling phenomena on the heater surface occur 1.3 mm away from the thermocouple hole. The actual wall temperature was obtained using a one-dimensional heat conduction equation in the radial direction, as demonstrated in Eq. (2):

$$T_w = T_{thermo} - \frac{Q}{2\pi L}\left[\frac{\ln(r_o/r_{thermo})}{k_{\text{test}}}\right] \tag{2}$$

where T_w, T_{thermo}, L, r_o, r_{thermo}, and k are wall temperature, temperature measured by thermocouples, heater length, outside radius, radius of thermocouple location, and thermal conductivity of heater, respectively.

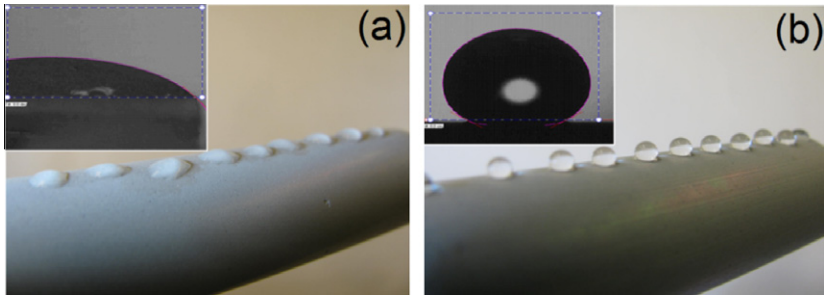

Fig. 3. Water contact angle: (a) ASNPS and (b) SASNPS (inset shows WCA on the flat samples, 50° and 150°, respectively).

In order to obtain the local heat transfer coefficient (HTC), the corrected wall temperature from Eq. (2) was plugged into Eq. (3):

$$h = \frac{Q/A}{(T_w - T_{sat})} \tag{3}$$

The average heat transfer coefficient was given by averaging the four local heat transfer coefficients determined by Eq. (3) as shown below:

$$h_{\text{mea}} = \frac{h_{top} + h_{left} + h_{right} + h_{bottom}}{4} \tag{4}$$

Nominal uncertainty of T-type thermocouple is ±0.5 °C and the voltage and current measurement uncertainties are ±0.5 V and ±0.04 A, respectively. The uncertainty is estimated by Moffat [21] as shown in Eqs. (5) and (6):

$$\Delta q'' = \sqrt{\left(\frac{\partial q''}{\partial w}\Delta w\right)^2 + \left(\frac{\partial q''}{\partial r}\Delta r\right)^2 + \left(\frac{\partial q''}{\partial L}\Delta L\right)^2} \tag{5}$$

$$\Delta h = \sqrt{\left(\frac{\partial h}{\partial q''}\Delta q''\right)^2 + \left(\frac{\partial h}{\partial T}\Delta T\right)^2} \tag{6}$$

The estimated uncertainties of power input and heat flux are within 8.1% and 8.6%, respectively.

3. Results and discussion

3.1. Water contact angle (WCA) hysteresis in nucleate pool boiling

It is well known that WCA hysteresis increases the chance to trap vapor in surface irregularities. A fundamental mechanism of vapor entrapment [31] is schematically illustrated in Fig. 4. When a liquid proceeds along a solid surface, the behavior of contact line along the downslope is determined by its advancing contact angle ϑa. For a hydrophobic surface (Fig. 4(a)), the liquid front will hit the opposite surface wall of the cavity before the contact line reaches the bottom of the indentation due to the equation $\vartheta_a > 2\beta$. The void space, which is not wetted by liquid, can entrap the vapor. For a hydrophilic surface (Fig. 4(b)), the nose of the liquid will move along the downslope due to the equation $\vartheta_a < 2\beta$. Relatively, the unwetted void space will be much smaller than that of a hydrophobic surface. One can expect similar phenomena when a liquid recedes on a solid surface. Additional vapor will be entrapped due to the fact $\vartheta_r > 180° - 2\beta$. When the solid surface is heated and the liquid temperature is raised, the entrapped vapor initiates the nucleate boiling at a lower superheat. However, a highly-wetted solid surface requires a much higher superheat to entrap the vapor.

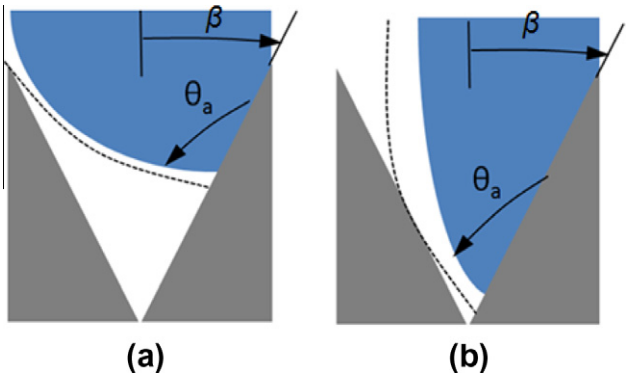

Fig. 4. Schematic illustration of proceeding liquid on the porous surface [31]: (a) hydrophobic (non-wetting) surface and (b) hydrophilic (wetting) surface.

In order to visualize the WCA hysteresis, an immersion and removal test using slabs with plain, ASNPS, and SASNPS were carried out. First, a plain thin slab (thickness 2 mm) was very slowly vertically immersed in water and then stopped to reach the equilibrium contact angle. Similarly, the slab was vertically withdrawn from water very slowly and stopped. As shown in Fig. 5(a), a plain surface does not show any specific WCA hysteresis. The same test was carried out for ASNPS and SASNPS formulas. For the ASNPS slab, the ϑ_a and ϑ_r in Fig. 5(b) are larger than that of a plain surface. Since the ASNPS is a highly wetting surface, water is instantly absorbed by the capillary force made stronger through interconnected pores. The contact angle hysteresis ($\vartheta_a - \vartheta_r < 90$) is observed for the ASNPS slab and is compared to that of plain slab ($\vartheta_a - \vartheta_r \sim 90$). In contrast the numerous nano pores on the SASPS rarely become wet while the slab advanced and receded. The contact angle hysteresis ($\vartheta_a - \vartheta_r \gg 90$) observed for the SASNPS slab is much larger when compared to that of the ASNPS slab ($\vartheta_a - \vartheta_{ar} > 90$) in Fig. 5(c).

To check the surface of the pore mouth, an Atomic Force Microscopy (AFM) was carried out. As shown in Fig. 6, the pore wall is quite steep and the depth is at least ~200 nm. Due to its reduced surface wettability, the water is not easily penetrated into the pores of the SASNPS. The steep walls enable more vapors to be entrapped than typical conical cavity. This finding implies that the SASNPS facilitates the nucleate boiling incipience at much lower superheat.

3.2. Nucleate pool boiling of the ASNPS and the SASNPS

In the nucleate pool boiling experiment, three different surface-treated Al 6061 test sections were used: plain surface, ASNPS, and SAM-coated ASNPS (SASNPS). The boiling curves for different surface-treated structures are shown in Fig. 7(a). The single-phase natural convection heat transfer at lower heat flux regimes ($q'' < 20$ kW/m^2) is included. For the ASNPS, the boiling curve shifts to the left throughout the nucleate region when compared to that of the plain surface. The Onset of Nucleate Boiling (ONB) is observed at ΔT of 3.5 K, which is approximately 4 K lower than that of the plain surface (7.5 K). A significantly reduced ONB could be ascribed to entrapped vapor through the large internal pore surface area; vaporization occurred within the nano-porous matrix. At a lower heat flux regime (20 kW/m^2 < q'' < 40 kW/m^2), the heat transfer coefficient (HTC) enhancement is approximately ~200% and the HTC augment within 40 kW/m^2 < q'' < 100 kW/m^2 is ~75% when compared to that of the plain surface. A significant HTC enhancement at a low heat flux regime is also ascribed to the enhanced surface area and assists the vapor generation inside the pore. Typically, on the highly wetted ASNPS, the liquid protrudes into the pore and forms an ultra-thin liquid film. Eventually, the wetting ability facilitates the evaporation inside the pore media. The interior vapor is transported via the macro-level outside cavities [22]. Another contributing factor of the evaporation is a combination of the internal and external convection through the porous matrix. In Fig. 7(b), the bubble generated from the heater surface is evenly distributed along the heater peripheries. We observed that the departing bubble diameter d_b is relatively smaller than that of the plain surface bubble. It is assumed that the reduced interfacial contact angle on the ASNPS prohibits the bubble merging and increases the bubble departure frequency f_b. When the bubbles are departed from the surface, the liquid is pumped in and out the porous medium, which, in turn, induces the internal convection inside the porous structure. The departing bubbles, which agitate and disturb the thermal boundary layer, lead to the external convection. At a high heat flux regime, the increase of the wall superheat is still suppressed when compared to that of the plain surface. In the previous study [23], the most of active

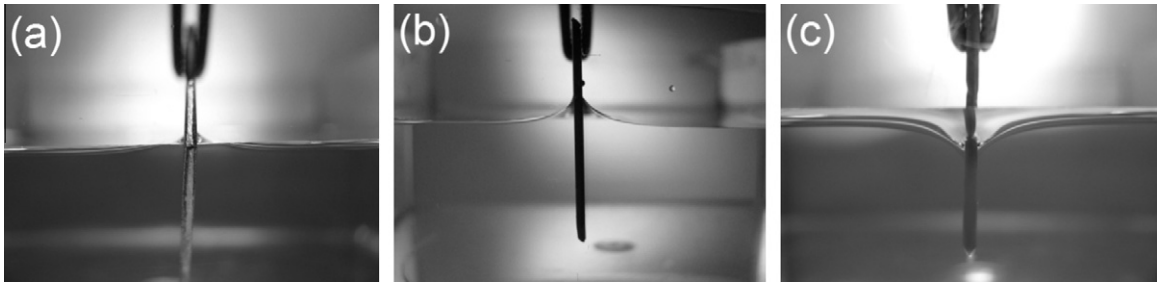

Fig. 5. Slab (thickness 2 mm) immersion test for water contact angle hysteresis: (a) plain surface (b) ASNPS and (c) SASNPS.

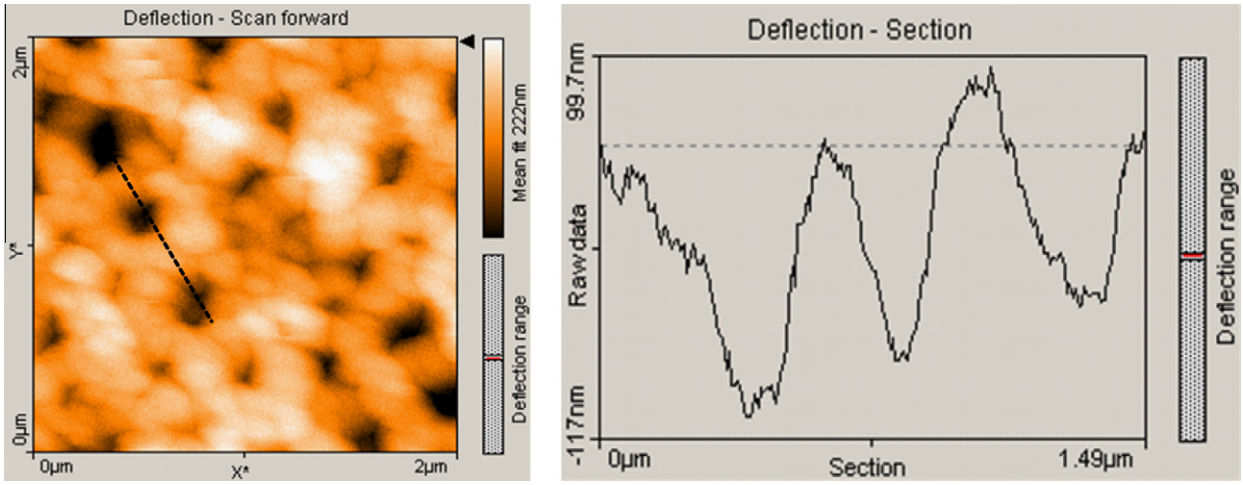

Fig. 6. (a) AFM (deflection mode) images of ASNPS and (b) cross-section view of nano pores.

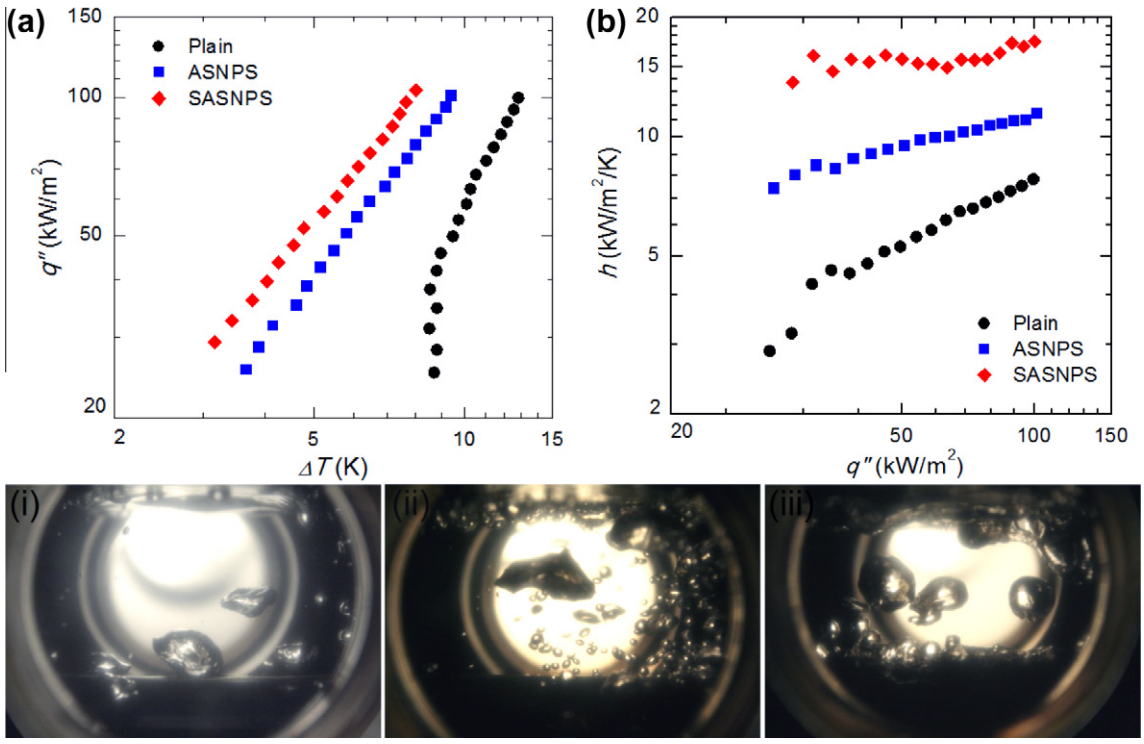

Fig. 7. Pool boiling curves (a) heat flux vs. wall superheat and (b) HTC vs. heat flux: the bubble motion sat different heat flux: (i) plain surface, (ii) the ASNPS, and (iii) the SASNPS at $q'' = 20\ kW/m^2$.

nucleation site densities at a high heat flux were diminished by the vapor blanket layer formation due to the bubble coalescence at the 1-D nano pore (Fig. 2(a), $d_p \sim 30$ nm). However, seemingly the ASNPS does not show the HTC deterioration caused by vapor blanketing. The reduced bubble diameter caused by the effective wetting of the ASNPS prevents the bubble coalescence on the ASNPS. As the wall superheat increases, the bubble departure diameter increases and leads to a considerable "bubble sweeping" along the cylindrical heater peripheries. The HTC augmentation caused by the bubble sweeping is more prominent on the cylindrical heater rather than the flat heater. Also, it is postulated that three dimensional porous network facilitates the vapor–liquid counter flow. It was observed the vapor bubbles escape from the large pore, whereas the liquid flows through the porous walls, assisted by the capillary suction.

For the SASNPS, the boiling curve shifts to the far left when compared to those of the plain and the ASNPS in Fig. 7(a). The ONB is significantly decreased and observed at ~2 K. This could be closely related to the active nucleation site density increase, which is due to the poorly-wetted (hydrophobic) surface. The amount of entrapped vapor is proportional to the interstitial volume. The vapor inside the pore for the SASNPS commences the nucleate boiling incipience at a much lower superheat than that of the ASNPS. The HTC augment is ~300% at lower heat flux regime ($20\ \text{kW/m}^2 < q'' < 40\ \text{kW/m}^2$) and the HTC in the range of $40\ \text{kW/m}^2 < q'' < 100\ \text{kW/m}^2$ is ~190% compared to that of the plain surface. The significant HTC enhancement is probably due to both the increased surface area and the intensified nucleation site densities.

Wang and Dhir proposed the correlation of the number of active nucleate site density, which can be expressed as a function of contact angle [17]:

$$N_a = N_c(1 - cos\theta)\Delta T \tag{7}$$

where N_a, N_c, θ, and ΔT are the number of active nucleate site density, the number of cavities per unit surface area, contact angle, and wall superheat at given heat flux.

Eq. (7) shows reasonable results for the experimental data within 60% error ($10° < \vartheta < 90°$). In order to estimate the effective enhancement of N_a, the same number of N_c is assumed at a given superheat for the ASNPS and SASNPS. The effective enhancement of N_a is estimated approximately 2.3 times: $(N_{a,\text{SASNPS}} - N_{a,\text{ASNPS}})/N_{a,\text{ASNPS}} = 2.35$, $\theta_{\text{SASNPS}} = 150°$, $\theta_{\text{ASNPS}} = 50°$. The intensified number of active nucleate side density can be approximately compared by visualized number of bubble on the surface in Fig. 7.

In addition, the bubble motion is influenced by the interfacial contact angle (see Fig. 8). Due to the poor wetting (hydrophobic) surface, the surface tension force reduces the bubble neck formation. The spread bubble on the pore mouth, can coalescence easily to the adjacent bubble. Therefore, the departure bubble's diameter is much larger whereas the bubble departure frequency is much smaller. Fritz predicted the bubble departure diameter by using the fundamental properties of liquid. It can be expressed by the wettability change while bubble grows [24]:

$$d_b = 0.0208\theta\sqrt{\sigma/g(\rho_l - \rho_v)} \tag{8}$$

where d_b is the bubble departure diameter, ϑ is contact angle, σ is surface tension, g is gravitational force, ρ_l and ρ_v are liquid and vapor densities, respectively.

Eq. (8) can capture the influence between the surface wetting and the departure bubble diameter. When two adjacent bubbles, with the same size merge with each other, the resulting bubble has two times larger volume but the diameter increases only 26% [7]. The buoyancy force of the merged bubble can immediately overcome the surface-tension retention force and detach the bubble from the heating surface. The larger volume of bubbles can remove more latent heat from the heating surface and induce a highly intensified convective flow. After the larger bubble lift-off, the amount of liquid pumped in and out the porous medium is larger than that of the smaller one. This is heavily due to the interconnected passages which facilitate fresh liquid into the pore through the liquid intake process. The fresh liquid infiltration reduces the wall superheat even at a high heat flux region. For the external convection, the enhanced turbulence and eddies are induced by a number of departing bubbles and lead to the disturbance of the thermal boundary layer. Similar to the ASNPS, there is no HTC deterioration observed at a higher heat flux regime ($40\ \text{kW/m}^2 < q\prime < 100\ \text{kW/m}^2$). This phenomenon can be closely related to the bubble motion. Typically, the bubble departure diameter gradually increases as the heat flux increases. Cole proposed the correlation between d_b and f_b by using liquid properties [25]:

$$f_b d_b = 0.59\left[\frac{\sigma g(\rho_l - \rho_v)}{\rho_l^2}\right]^{0.25} \tag{9}$$

$$Bo^{1/2} = 0.04Ja \tag{10}$$

$$Ja = \frac{(T_w - T_{sat})c_{pl}\rho_l}{\rho_v h_{lv}} \tag{11}$$

$$d_b = \left[\frac{\sigma Bo}{g(\rho_l - \rho_v)}\right]^{1/2} \tag{12}$$

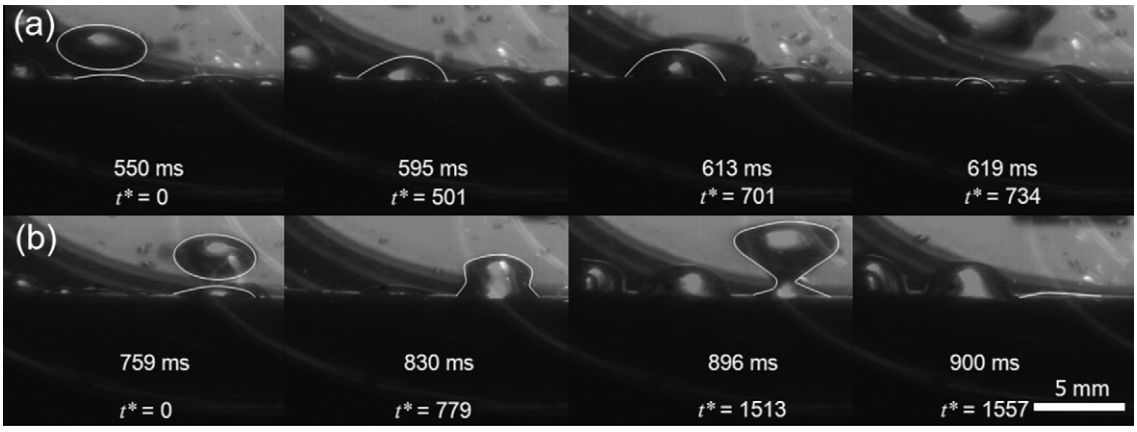

Fig. 8. Departing bubble motions on the SASNPS at $q'' = 20\ \text{kW/m}^2$: (a) bubble departed by adjacent bubble (bubble sweeping) and (b) single bubble departure.

where σ, g, ρ_l, ρ_v, Bo, Ja, c_{pl}, and h_{lv} are surface tension, gravitational force, liquid and vapor densities, Bond number, Jakob number, heat capacity, and latent heat, respectively.

Since d_b and f_b of the single bubble motion are inversely correlated each other in Eq. (9), the HTC augment of the SASNPS cannot be elucidated by assuming the bubble motion follows Eq. (9). The enlarged bubble departure diameter leads to reduced bubble departure diameter due to the extended bubble waiting time before it leaves the surface. However, for the cylindrical heating surface, the bubble sweeping along the peripheries has a substantial waiting time. This long departure time contributes to the HTC augmentation at a higher heat flux regime. The consecutive bubble motions of the SASNPS, taken by a high speed camera, highlight the importance of the bubble sweeping. For comparison, the reduced time is used rather than a real time scale [26]. The bubble lifts-off from the heating surface at $t^* = 0$ ($t = 550$ ms). The departing bubble leaves a thin vapor layer on the hydrophobic surface. The remaining vapor layer can easily initiate the bubble formation with a small amount of superheat. When the bubble grows hemispherically ($t^* = 701$, $t = 613$ ms), the departing bubble from the bottom suddenly coalescences. Then, it becomes a much larger bubble and detaches immediately due to increased buoyancy force ($t^* = 734$, $t = 619$ ms). After the bubble detachment, the thin vapor layer remains on the surface. Similarly, the adjacent departing bubble has a residue of a thin vapor layer ($t^* = 0$, $t = 759$ ms). At $t^* = 779$ ($t = 830$ ms) the bubble is not detached from the surface due to thick bubble neck caused by strong surface-tension retention force on the hydrophobic surface. The bubble has to wait until the buoyancy force overcomes the surface tension force until at $t^* = 1557$ ($t = 900$ ms). This finding demonstrates that the single bubble on the hydrophobic surface takes a much longer time (two times slower) without the assistance of adjacent drifting bubbles in the pool. It should be noted that the bubble sweeping action is important for the cylindrical heater. From the observation of the bubble motion, the bubble departure diameter and bubble departure frequency are influenced by surface tension as well as the force balance between the interfaces (liquid, vapor, and solid). It means that Eq. (11) may not be sufficient to describe the bubble motion on the heating surface with different wetting applications using surface tension alone. Eventually, the correlation of the bubble

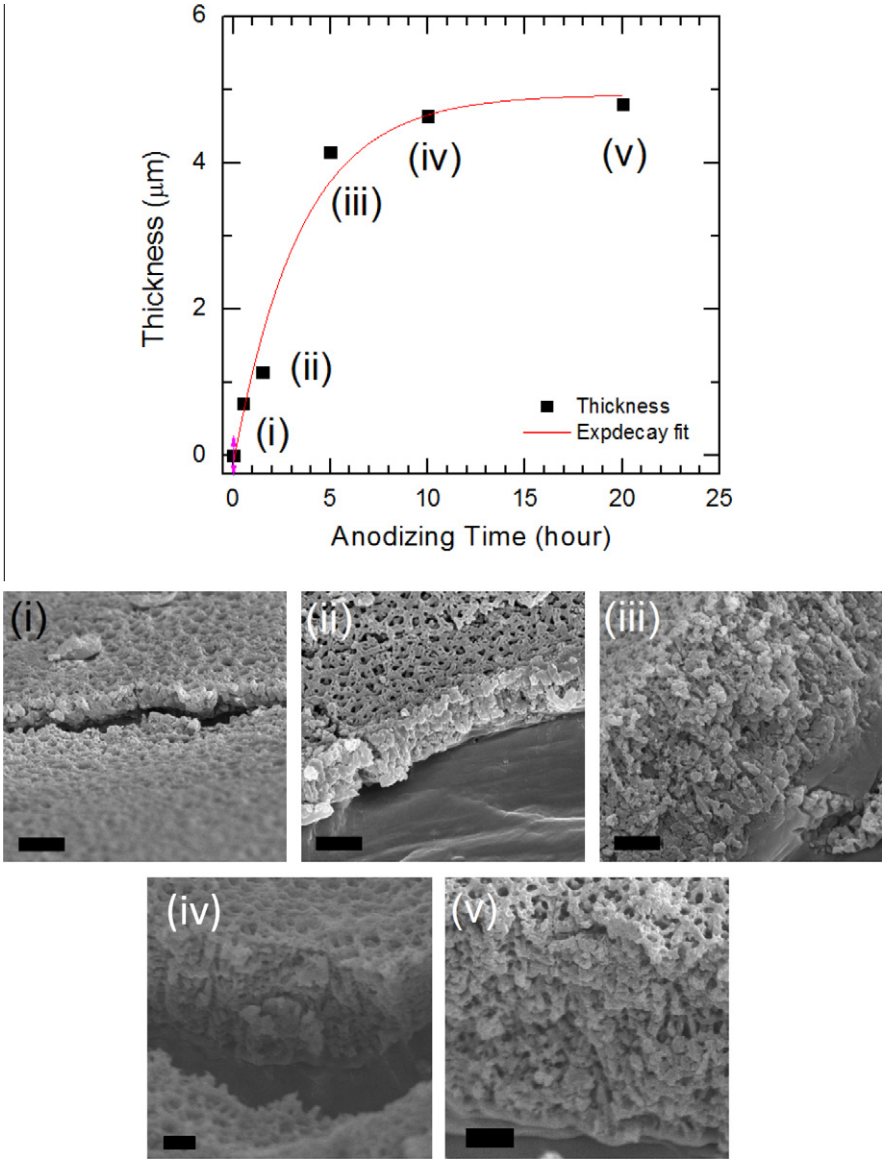

Fig. 9. A plot of the ASNPS thickness over the anodizing time. SEM images of the ASNPS fabricated in 0.3 M phosphoric acid at 140 V with different reaction times: (a) 0.5 h, (b) 2 h, (c) 6 h, (d) 10 h, and (e) 20 h. Scale bar represents 1 μm.

motion should be modified with respect to not only surface tension but also to the interfacial contact angle.

3.3. Effect of thickness of the ASNPS in nucleate pool boiling

In Section 3.2, the augmented boiling phenomena are observed at different surface-treated structures such as three dimensionally interconnected porous structure and the hydrophobic coated surface. It is assumed that an enlarged surface area and an enhanced number of the active nucleate site density are the dominant contributing factors, which can proportionally increase the thickness of the ASNPS. Contrary to this finding, a thicker coating might deteriorate the boiling performance due to increased thermal resistance. The thermophysical properties of metal dramatically change after a metal oxide formation. Therefore, the optimal thickness of metal, oxide based porous surfaces might be an important issue to escalate the boiling performance induced by an enhanced surface area and an active nucleate site density. In this section, the boiling experiment results with different thicknesses of the ASNPS are investigated to find the optimal condition. The thickness of the ASNPS is usually proportional to the anodizing reaction time and the anodizing voltage applied. Therefore, the anodizing reaction time is crucial and investigated in this study. In order to estimate the thickness of the ASNPS, SEM images of each of the cross-sectional views were taken. Based on the SEM images, the thickness of the ASNPS was plotted over the anodizing time and is shown in Fig. 9.

In early stage of anodizing, the thickness growth rate shows a steep slope up to 6 h (~0.75 μm/h). As anodizing reaction time increases, the thickness growth rate begins to saturate. Eventually, after ten hours, there is no significant difference observed in mean thicknesses of the ASNPS.

The boiling curves of the ASNPS with different thickness are shown in Fig. 10. As the thickness increases up to two hours, the boiling curves shift to the left hand side when compared to that of the plain surface. The maximum HTC enhancement at a lower heat flux regime ($q'' < 40\ kW/m^2$) is observed for the ASNPS at two hours. Interestingly, the maximum HTC at a higher heat flux regime ($q'' > 60\ kW/m^2$) is achieved by the ASNPS at 0.5 h. At a lower heat flux regime, the number of the active nucleate site density is a contributing factor to enhance the boiling phenomena. On the contrary, at a high heat flux regime, bubbles generated from the numerous active nucleate site densities might suppress the heat transfer via bubble coalescence, leading to vapor blanketing. The respective of heat transfer, with a thickness of a few microns, is not critical enough to deteriorate the boiling phenomena. This finding indicates the HTC augment is achieved by increasing the surface area and the number of active nucleate side densities, which compensate for the increased thermal resistance. However, beyond a certain anodizing time of 20 h, the HTC becomes much less than that of the plain surface due to lower thermal conductivity and vapor departure resistance. The HTC trends of the ASNPS at different reaction times are clearly observed at visualization of the cylindrical heater surface.

As can be seen in Fig. 10, numerous bubble nucleations are observed. However, for the ASNPS at 20 h, there is no significant bubble formations observed, which is very similar to that of the plain surface after 20 h. These phenomena might due to the reduced heating surface area and poor thermal conductivity. Malyshenko [36] reported that the vapor film thickness near the heating surface was approximately half the thickness of the porous coating at a high heat flux regime. Another factor is vapor departure resistance inside the porous media. If the vapor is stagnant inside thick porous coating due to departure resistance, it plays the role of

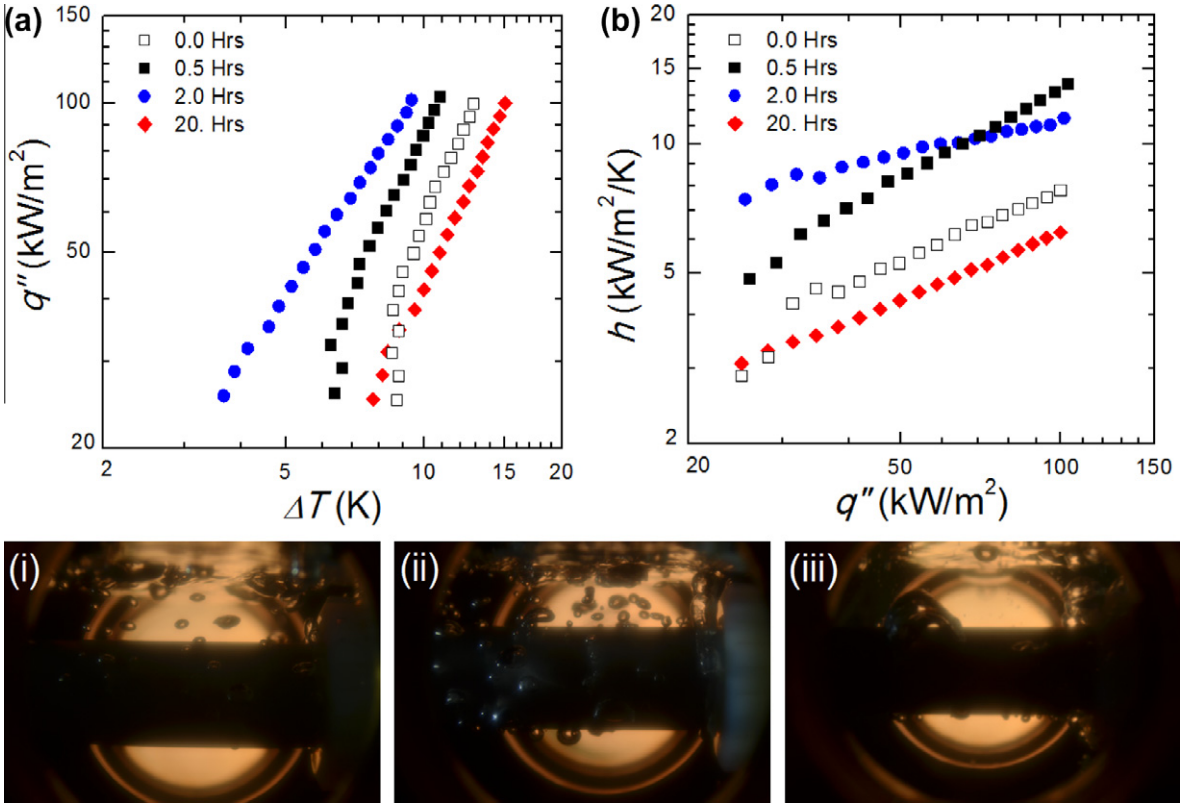

Fig. 10. Effect of ASNPS thickness on pool boiling curves arising from anonizing time (a) heat flux vs. wall superheat and (b) HTC vs. heat flux: the bubble motions at different heat flux: (i) 0.5 h, (ii) 2 h, and (iii) 20 h at $q'' = 20\ kW/m^2$.

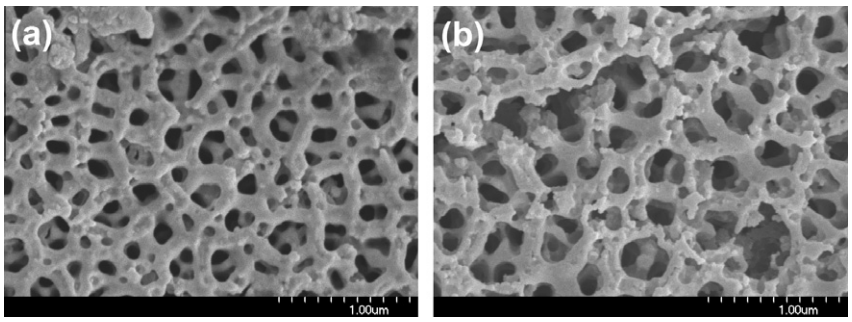

Fig. 11. Boiling in water for 2 h: (a) ASNPS and (b) SASNPS.

insulation because of its poor thermal conductivity. Also, the thick coating prohibits mass transport and fresh liquid infiltration into the pores. Therefore, the wall superheat significantly increases. Meléndez and Reyes [27] and Yang et al. [9] reported similar phenomena at larger foam cover thickness.

Relating to heat transfer deterioration, the aging effect should be mentioned In pool boiling of the aluminum-based heating surface. Alumina is vulnerable to further oxidation in aqueous pool boiling and accompanies morphology change. Eventually, the morphology change leads to the active cavity decrease. Fig. 11 shows the heating surface of the ASNPS and SASNPS after 2 h boiling in water. Within a short time, it seems no significant aging propagation. However, for longer period runs, individual cavities begin to be clogged by further oxidation, which was clearly shown in previous study [37]. In order to prevent aging phenomena, pool boiling in non-aqueous liquid would prevent and/or retard morphology change.

3.4. Mechanistic model proposals

Pool boiling correlations are a useful tool to predict the nucleate boiling heat transfer in engineering systems. Numerous investigators have proposed various correlations with respect to their own mechanistic model. One of the widely used correlations is Rohsenow's correlation, which is based on forced-convection processes [28]:

$$q'' = C_{sf}^{-1/r} Pr^{-s/r} \mu i_{lv} \left[\frac{g(\rho_l - \rho_v)}{\sigma}\right]^{1/2} \left[\frac{c_{pl}(T_w - T_{sat})}{i_{lv}}\right]^{1/r} \quad (13)$$

where Pr, μ, h_{lv}, g, ρ, σ, and c_{pl} are Prandtl number, viscosity, enthalpy, gravitational acceleration, density, surface tension, and heat capacity, respectively.

C_{sf}, r, and s are empirically determined values. Initially, Rohsenow recommended $r = 0.33$, $s = 1.7$. C_{sf} in Eq. (12) represent interactions of the liquid–solid surface. However, each combination of a liquid–solid has different value. Vachon et al. [29] invested C_{sf} values of various liquid–solid combinations, which has been used useful indicators for the particular combinations. If the value of C_{sf} is not tabulated, typically, $C_{sf} = 0.013$, which represents a water–copper combination and is recommended for plain surface. Frequently, C_{sf} has been used to indicate surface "roughness". Typically, the lower value of C_{sf} represent a rougher surface.

The Rohsenow model is correlated to pool boiling experimental data of different surface-treated heaters in Fig. 12(a). For the plain surface, the empirically obtained C_{sf} value is 0.0047, significantly smaller than the recommended value of 0.013. The experimental data is relatively well-correlated with an 18% deviation. On the contrary, porous structured-surfaces such as ASNPS and SASNPS show significant deviations even with a wide range of C_{sf}. Since Rohsenow developed Eq. (12) based only on the forced-convection in the nucleate boiling, it may not be sufficient to describe the boiling characteristics of porous surfaces. Nakayama et al. [4] proposed the correlation which will be usable for porous surfaces; it combines the contribution of porous coating and forced-convection:

$$q'' = \left(\frac{\pi d_b^3}{6}\right) N'_a f_b h_{lv} \rho_v + \left(\frac{\Delta T}{C_q}\right)^{1/y} N_a'^{x/y} \quad (14)$$

where d_b, N'_a, f_b, h_{lv}, ρ, and ΔT are bubble departure diameter, number of active nucleate site density, bubble departure frequency, enthalpy, density, and wall superheat, respectively. Exponents x and y are given by 1 and 3 for the water system. Empirical value C_q is given by 1.95 for water.

The first term of the RHS of Eq. (14) represents a convection-driven heat transfer contribution and the second term of the RHS

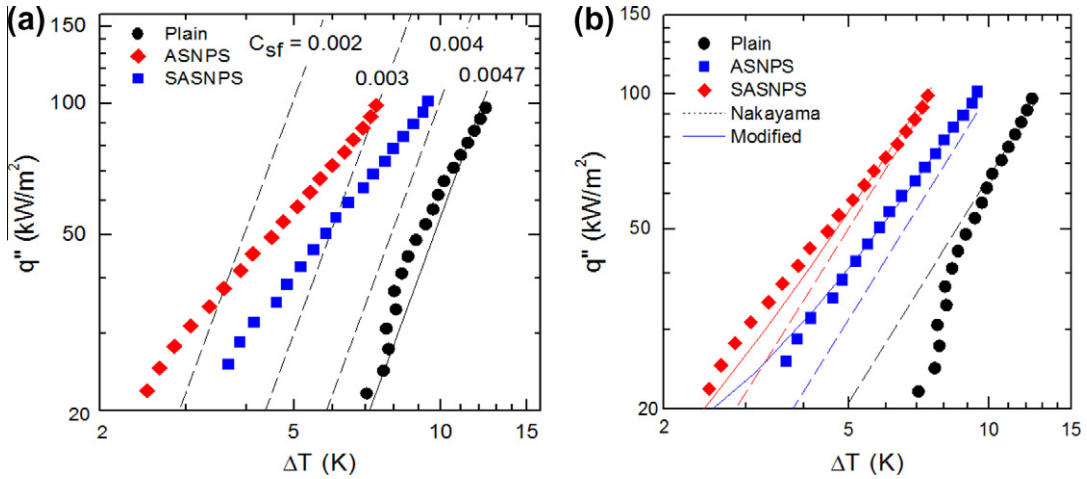

Fig. 12. Correlation of mechanistic models: (a) Rohsenow (dotted line), (b) Nakayama (dotted line) and modified (solid line).

represents the heat transfer contribution of the porous coating. In the first term, the latent heat is proportional to the volume of the bubble and the bubble departure frequency. In the original equation, the number of the active nucleate site density is empirically obtained by counting. As shown in Eq. (7), the number of the active nucleate site density is proportional to the wall superheat and the interfacial contact angle. Therefore, N'_a is replaced by N_a and used in Eq. (7). d_b and f_b are determined by visualization of the bubble departure at a specific surface in Eq. (14). In Fig. 12(b), the Nakayama correlation (dashed line) shows a strong similarity to the experimental data of the porous coatings with a 34–52% deviation. For the plain surface, the deviation at a lower heat flux regime is markedly large. It implies that the number of the active nucleation site density at a lower heat flux regime is overestimated. At the lower heat flux regime, the range of deviation is larger than the higher heat flux regime.

Another contributing factor could be the thin liquid film evaporation inside pores. Typically, the thin liquid film occurs at the corners of the pore mouth due to the vapor–liquid menisci. The segments of the thin liquid film separate the bubble formed inside the pore. The vapor constrained inside the pore grows because of the inertia force of the liquid adjacent to the bubble. The superheated vapor is generated and squeezed out of the pore. The pressure drop after the bubble departure causes fresh liquid to filtrate into the pore for next bubble cycle. This phenomenon is called the "suction–evaporation mode" [30]. The thin liquid film evaporation augments the evaporation heat transfer as well as the convective heat transfer. In order to compensate for the deviation of Eq. (14), the third term is added on the RHS in Eq. (14):

$$q'' = \left(\frac{\pi d_b^3}{6}\right) N'_a f_b i_{lv} \rho_v + \left(\frac{\Delta T}{C_q}\right)^{1/y} N_a'^{\,1/y} + \frac{C k_l \delta \Delta T}{(1-\cos\theta)} N_a'^{\,1/y} \qquad (15)$$

where k, δ, and C are thermal conductivity of liquid, thickness of thin film layer inside pore, and empirical constant, respectively.

Since the thin liquid film evaporation occurs at the active pores, N_a follows the same exponent in Eq. (14). The modified correlation (the solid line) of Eq. (15) with experimental data is shown in Fig. 12(b). The underestimated total heat transfer of Eq. (14) at a lower heat flux is compensated by the thin liquid film evaporation term and is better predicted (0.7–13%) than others described by Eqs. (13) and (14). This equation implies that the thin liquid film evaporation improves not only the total heat transfer but also the convective heat transfer for the ASNPS due to its significantly enhanced N_a.

4. Conclusion

In this study, the novel nano-porous structures fabricated by anodizing were studied in order to understand their effects on the heat transfers. By using the anodizing process, it was found that the efficient fabrication of the porous structure, due to anodizing, is promising in overcoming technical restrictions of the mechanical and chemical process. This can affect many aspects of fabrication, such as bulk fabrication, cost effectiveness, and the tailoring of precise surface pattering. Its characteristic boiling heat transfer enhancement was also reported on. One of the principal contributing factors is ascribed to the three-dimensionally interconnected porous networks. These networks enable an increase in the heat transfer surface area and the active nucleate site density. These networks entrap vapor inside the pore and lead to the suppression of the wall superheat heat increase. The thin liquid film evaporation (suction-evaporation mode) through numerous active nucleate site densities was also found to contribute to the HTC. In addition to its structural uniqueness, the surface wettability was modulated by the hydrophobic SAM, which improved more active pores by increasing the amount of vapor.

The influence of the thickness of the porous structure over the boiling heat transfer was investigated. The thinner ASNPS was beneficial in order to reduce the thermal resistance and vapor departure resistance but was not sufficient when increasing the surface area and the number of active nucleation sites. The thicker ASNPS was advantageous with respect to the surface area and the number of active nucleation sites. However, it was detrimental to the HTC due to increased thermal resistance and bubble departure resistance. In order to improve the HTC, the optimal thickness was preferential in pool boiling.

To adequately correlate the mechanistic model with experimentally obtained data, classical models such as Rohsenow and Nakayama were considered. Those correlations were not sufficient to adequately describe heat transfer phenomena of the ASNPS. We modified their correlations with the combination of forced-convection, the pore heat transfer, and the thin liquid film evaporation. The predicted boiling performance strongly correlated with the experimentally obtained boiling heat transfer in dealing with nano-porous surfaces.

Acknowledgments

This material is based upon work supported by the National Science Foundation under Grant No. 0923869 (STTR Phase II through Advanced Materials and Devices Inc., Reno, NV). K.J.K. also thanks partial financial support from the Korean Institute of Energy Research (KIER-B1-8135).

References

[1] M. Jakob, Heat Transfer, John Wiley and Sons, New York, 1949. pp. 636–638.
[2] C. Corty, A.S. Foust, Surface variables in nucleate boiling, Chem. Eng. Prog. Sym. Ser. L2051 (1955) 1–12.
[3] P.J. Marto, W.M. Rohsenow, Effects of surface conditions on nucleate pool boiling of sodium, ASME J. Heat Transfer 88 (1966) 196–204.
[4] W. Nakayama, T. Daikoku, H. Kuwahara, T. Nakajima, Dynamic model of enhanced boiling heat transfer on porous surfaces, ASME J. Heat Transfer 102 (1980) 445–450.
[5] A.E. Bergles, M.C. Chyu, Characteristics of nucleate pool boiling from porous metallic coatings, ASME J. Heat Transfer 104 (1982) 279–285.
[6] J.P. O'Connor, S.M. You, A painting technique to enhance pool boiling heat transfer in FC-72, ASME J. Heat Transfer 117 (1995) 387–393.
[7] J.H. Kim, K.N. Raney, S.M. You, J.Y. Pak, Mechanism of nucleate boiling heat transfer enhancement from microporous surfaces in saturated FC-72, ASME J. Heat Transfer 124 (2002) 500–506.
[8] S. Mori, K. Okuyama, Enhancement of the critical heat flux in saturated pool boiling using honeycomb porous media, Int. J. Multiphas. Flow 35 (2009) 946–951.
[9] Y. Yang, X. Ji, J. Xu, Pool boiling heat transfer on copper foam covers with water as working fluid, Int. J. Therm. Sci. 49 (2010) 1227–1237.
[10] Y.Y. Hsu, On the size range of active nucleation cavities on a heating surface, ASME J. Heat Transfer 84 (1962) 207–216.
[11] S. Launay, A. Fedorov, Y. Joshi, A. Cao, P. Ajayan, Hybrid micro-nano structured thermal interface for pool boiling heat transfer enhancement, Microelectron. J. 37 (2006) 1158–1164.
[12] C. Li, Z. Wang, P.-I. Wang, Y. Peles, N. Koratkar, G.P. Peterson, Nano structured copper interfaces for enhanced boiling, Small 4 (2008) 1084–1088.
[13] P. Griffith, J.D. Wallis, The role of surface conditions in nucleate boiling, Chem. Eng. Prog. Symp. Ser. 56 (1960) 49–63.
[14] R.L. Hummel, Means for increasing the heat transfer coefficient between a wall and boiling liquid, U.S. Patent, 3207209, 1965.
[15] R.F. Gaertner, Methods and means for increasing the heat transfer coefficient between a wall and boiling liquid, U.S. Patent, 3301314, 1967.
[16] R.I. Vachon, G.H. Nix, G.E. Tanger, R.E. Cobb, Pool boiling heat transfer from Teflon-coated stainless steel, ASME J. Heat Transfer 91 (1969) 364–370.
[17] C.H. Wang, V.K. Dhir, Effect of surface wettability on active nucleation site density during pool boiling of water on a vertical surface, ASME J. Heat Transfer 115 (1993) 659–669.
[18] M. Curioni, P. Skeldon, J. Ferguson, G.E. Thompson, Reducing the energy cost of protective anodizing, J. Appl. Electrochem. 41 (2011) 773–785.
[19] D. Kim, K. Lee, P. Roy, B.I. Birajdar, E. Spiecker, P. Schmuki, Formation of a non-thickness-limited titanium dioxide mesosponge and its use in dye-sensitized solar cells, Angew. Chem. Int. Ed. 48 (2009) 9326–9329.

[20] N.K. Allam, C.A. Grimes, Electrochemical fabrication of complex copper oxide nano architectures via copper anodization in aqueous and non-aqueous electrolytes, Mater. Lett. 65 (2011) 1949–1955.
[21] Moffat, Using uncertainty analysis in the planning of an experiment, J. Fluids Eng. 107 (1985) 173.
[22] R. Furberg, B. Palm, S. Li, M. Toprak, M. Muhammed, The use of a nano- and microporous surface layer to enhance boiling in a plate heat exchange, ASME J. Heat Transfer 131 (2009) 101010-1–101010-8.
[23] C.Y. Lee, M.M.H. Bhuiya, K.J. Kim, Pool boiling heat transfer with nano-porous surface, Int. J. Heat Mass Transfer 53 (2010) 4274–4279.
[24] W. Fritz, Phys. Z. 36 (1935) 379–384.
[25] R. Cole, W.M. Rohsenow, Correlations for bubble departure diameters for boiling of saturated liquids, Chem. Eng. Prog. 65 (1969) 211–213.
[26] Y. Nam, J. Wu, G. Warrier, Y.S. Ju, Experimental and numerical study of single bubble dynamics on a hydrophobic surface, ASME J. Heat Transfer 131 (2009) 121004-1–121004-7.
[27] E. Meléndez, R. Reyes, The pool boiling heat transfer enhancement from experiments with binary mixtures and porous heating covers, Exp. Therm. Fluid Sci. 30 (2006) 185–192.
[28] W.M. Rohsenow, A method of correlating heat transfer data for surface boiling of liquids, Trans. ASME 74 (1952) 9699–9975.
[29] R.I. Vachon, G.H. Nix, G.E. Tanger, Evaluation of constants for the Rohsenow pool-boiling correlation, ASME J. Heat Transfer 90 (1968) 239–247.
[30] Y.Y. Jiang, W.C. Wang, D. Wang, B.X. Wang, Boiling heat transfer on machined porous surfaces with structural optimization, Int. J. Heat Mass Transfer 44 (2001) 443–456.
[31] V.P. Carey, Liquid–Vapor Phase-Change Phenomena: An Introduction to the Thermo physics of Vaporization and Condensation Processes in Heat Transfer Equipment, Hemisphere Publishing Corporation, Washington, 1992.
[32] S.S. Hsieh, C.G. Ke, Bubble dynamic parameters and pool boiling heat transfer on plasma coated tubes in saturated R134a and R-600a, ASME J. Heat Transfer 124 (2002) 704–716.
[33] J.T. Cielslinski, Nucleate pool boiling on porous metallic coatings, Exp. Therm. Fluid Sci. 25 (2002) 557–564.
[34] K.N. Rainey, S.M. You, Plain and microporous, square pin-finned surfaces in saturated FC-72, ASME J. Heat Transfer 122 (2000) 509–516.
[35] M.S. El-Genk, A. El-Genk, A.F. Ali, Enhanced nucleate boiling on copper micro-porous surfaces, Int. J. Multiphase Flow 36 (2010) 780–792.
[36] S.P. Malyshenko, Features of heat transfer with boiling on surfaces with porous coating, Therm. Eng. 38 (2) (1991) 81–88.
[37] C.Y. Lee, B.J. Zhang, K.J. Kim, Morphological change of plain and nano-porous surfaces during boiling and its effect on nucleate pool boiling, Exp. Therm. Fluid Sci. 40 (2012) 150–158.